# Structure refinement, hydrogen-bond system and vibrational spectroscopy of hohmannite, $Fe_2^{3+}[O(SO_4)_2]\cdot 8H_2O$

G. Ventruti[1],*, G. Della Ventura[2], R. Orlando[3] and F. Scordari[1]

[1] Dipartimento di Scienze della Terra e Geoambientali, Università di Bari, via Orabona, 4, I-70125 Bari, Italy
[2] Dipartimento Scienze, Università di Roma Tre, Largo S. Leonardo Murialdo 1, I-00146 Rome, Italy
[3] Dipartimento di Chimica, Università di Torino, Via P. Giuria 5, Turin I-10125, Italy

**ABSTRACT**

The crystal structure of hohmannite, $Fe_2^{3+}[O(SO_4)_2]\cdot 8H_2O$, was studied by means of single-crystal X-ray diffraction (XRD) and vibrational spectroscopy. The previous structural model was confirmed, though new diffraction data allowed the hydrogen-bond system to be described in greater and more accurate detail. *Ab initio* calculations were performed in order to determine accurate H positions and to support the experimental model obtained from XRD data. Infrared and Raman spectra are presented for the first time for this compound and comments are made on the basis of the crystal structure and the known literature for sulfate minerals.

## Introduction

HOHMANNITE, $Fe_2^{3+}[O(SO_4)_2]\cdot 8H_2O$, is a hydrous Fe-sulfate occurring in arid environments. It is found typically as a secondary product, associated with chalcanthite, metahohmannite, fibroferrite, sideronatrite and copiapite (Palache *et al.*, 1951) and originates from the chemical weathering and oxidation of primary Fe sulfides, such as pyrite or pyrrhotite, owing to bacterial action or to air-oxidation in hydrothermal and magmatic ore deposits (Bandy, 1938). At present there is an increasing interest in the scientific community for the study of Fe sulfates for various reasons. Firstly, Fe-bearing sulfates have been identified recently on Mars, with wide distributions and, locally, in large amounts, using both remote sensing spectroscopic observations and direct-surface explorations by rovers (e.g. Klingelhöfer *et al.*, 2004; Johnson *et al.*, 2007; Vicenzi *et al.*,

2007; Lane *et al.*, 2008; Mills *et al.*, 2013; McCollom *et al.*, 2014). Secondly, these sulfates originate as an intermediate step in a complex series of oxidation, dehydration and neutralization reactions culminating in the precipitation of Fe oxyhydroxides (Jerz and Rimstidt, 2003; Burns, 1987); these processes are associated with AMD (acid mine drainage) and result in the outflow of acidic water from metal- or coal-mine wastes, thus representing a significant environmental concern (e.g. Nordstrom *et al.*, 2000; Welch *et al.*, 2007, 2008, 2009). Iron-sulfate concentrations are common in base-metal deposits, coal deposits, tailings and waste-rock piles, and are related spatially to oxidizing Fe-sulfide minerals. Their considerable solubility causes Fe-sulfate minerals to be found in sheltered sites such as rock overhangs (thereby protected from rain dissolution), or during drier times of the year, as a consequence of the migration of Fe-sulfate solutions to the surface and subsequent evaporation (Jerz and Rimstidt, 2003). Therefore these compounds are sensitive indicators of environ-

mental conditions such as pH, relative humidity, oxygen activity and sulfate activity. Hohmannite, together with other metal-bearing sulfates, is, additionally, involved in industrial processes, as a product of the corrosion of carbon steels (Ruhl and Kranzmann, 2012) and as an intermediate product in the treatment of metal residues from hydrometallurgic plants (Ngenda *et al.*, 2009).

Iron-bearing sulfates are difficult to characterize because they occur typically as loose, poorly coherent, powdery masses, making their detection using single-crystal XRD techniques problematic. For this reason, structural investigations on hohmannite are limited. Vibrational spectroscopy techniques are extremely useful in this context (Della Ventura *et al.*, 2013; Ventruti *et al.*, 2013) because they can provide a rapid

identification of the sulfate phase from both powders and single crystals; they are also able to provide a detailed characterization of the degree of hydration of the phase, which is essential for a rigorous interpretation of the hydrologic history of the environment.

To date, no spectroscopic studies have been reported for hohmannite. Its crystal structure was solved firstly by Scordari (1978) starting from a three-dimensional Patterson synthesis, whereas the geometry and positions of the hydrogen bonds were inferred only from geometrical considerations. The aim of the present work is to provide a complete and detailed characterization of the sample studied originally by Scordari (1978) by combining modern XRD with periodic *ab initio* calculations to describe the hydrogen-bonding

TABLE 1. Refined cell parameters and data-collection parameters for the hohmannite sample studied by single-crystal XRD.

**Crystal data**

| Crystal dimensions (mm) | | $0.320 \times 0.310 \times 0.040$ |
|---|---|---|
| Crystal system | | Triclinic |
| Space group | | $P\bar{1}$ |
| Unit-cell dimension | $a$ (Å) | 9.1428(2) |
| | $b$ (Å) | 10.9346(3) |
| | $c$ (Å) | 7.2168(2) |
| | $\alpha$ (°) | 90.547(1) |
| | $\beta$ (°) | 90.612(1) |
| | $\gamma$ (°) | 107.375(1) |
| Volume (Å$^3$) | | 688.46(3) |
| $Z$, $\rho_{calc}$ (g·cm$^{-3}$) | | 2, 2.238 |
| $\mu$ (mm$^{-1}$) | | 2.50 |
| F(000) | | 472 |

**Data collection and refinement**

| $\theta$ range for data collection (°) | 2 to 38.0 |
|---|---|
| Index range | $-15 \leqslant h \leqslant 15$, $-18 \leqslant k \leqslant 18$, $-12 \leqslant l \leqslant 12$ |
| Completeness | 98.0% |
| Max. and min. transmission | 0.629, 0.747 |
| Reflections collected/independent | 24,651/7183 |
| $R$ merging [$R_{(int)}$] (%) | 2.24 |
| Reflections used | 5787 with $I > 3\sigma(I)$ |
| No. of refined parameters | 238 |
| Gof[a] | 0.76 |
| $R_1$[b] (on $F$) / $wR_2$[c] (on $F^2$) | 0.027/0.029 |
| $(\Delta/\sigma)_{max}$ | 0.001 |
| $\Delta\rho_{min}/\Delta\rho_{max}$(e/Å$^3$) | $-0.71/0.79$ |

[a] $= [\Sigma [w(F_o^2 - F_c^2)^2]/(n - p)]^{1/2}$, where $n$ is the number of reflections, $p$ is the total number of parameters refined and $w$ is the weighting scheme applied;
[b] $= R_1 = \Sigma[|F_o| - |F_c|]/\Sigma|F_o|$;
[c] $= wR_2 = [\Sigma[w(F_o^2 - F_c^2)^2]/\Sigma[w(F_o^2)^2]]^{1/2}$.

system. Vibrational (Fourier transform infrared (FTIR) and Raman spectroscopy) data are also presented and interpreted on the basis of this improved structural model.

## Experimental

The crystals investigated in this study were handpicked from the same rock specimen as studied by Scordari (1978) from the Sierra Gorda (Chile) deposit; thus the chemical composition is inferred to be the same as that reported in that study. A single crystal selected on the basis of its purity under a binocular microscope was mounted on a Bruker AXS APEXII diffractometer kappa-goniometer equipped with a 1K SMART CCD (charge coupled device) detector with a crystal-to-detector distance of 4 cm. The diffraction data were collected using monochromatic MoKα radiation and frame widths of 0.5º in ω, with 30 s acquisition time for each frame. A sphere of three-dimensional data was collected by employing an optimization strategy by the *Apex* program suite (Bruker, 2008) over the interval $4º \leqslant 2\theta \leqslant 76º$. The three-dimensional data were reduced and corrected for Lorentz, polarization and background effects by means of the Bruker program *SAINT-IRIX* (Bruker, 2008). Empirical absorption corrections were applied to all data on the basis of the intensities of equivalent reflections (Blessing, 1995) by means of the multi-scan method implemented in *SADABS* (Bruker, 2008). The structure refinement was performed in space group $P\bar{1}$ using the program *CRYSTALS* (Betteridge *et al.*, 2003) starting from the atomic parameters obtained by Scordari (1978). Reflections with $I > 3\sigma(I)$ were used for the structure refinement. Refined parameters were: atomic positions, atomic displacement parameters and overall scale factor. All atoms apart from hydrogen were refined anisotropically. The hydrogen atoms were located from the difference Fourier maps and refined independently by fixing the O−H distances at 0.85(3) Å and maintaining a dihedral angle H−O−H of ~104º. The isotropic atomic displacement parameters of hydrogen atoms were evaluated as $1.2*U_{eq}$ of the parent oxygen atom. Details on data collection, crystallographic data and refinement are given in Table 1. Atomic positions and displacement parameters for all non-hydrogen atoms are listed in Table 2. The refined positions of hydrogen atoms derived from difference-Fourier syntheses are given in Table 3. Selected interatomic distances are given in Table 4.

The electronic structure of the refined structure was calculated by means of a linear combination of atomic orbitals (LCAO) unrestricted Hartree-Fock (UHF) periodic computational scheme, using the *CRYSTAL09* program (Saunders *et al.*, 2003). For each atom a split-valence basis set was used. Optimization of exponents and coefficients was performed for the Gaussian-type valence orbital of S ions. To facilitate the convergence, the number of the unpaired electrons of $Fe^{3+}$ ions was locked in the first cycles of calculation. The cell parameters and the initial hydrogen positions adopted for each quantum-mechanical calculation were those determined by XRD.

For FTIR powder spectroscopy, samples were prepared as KBr pellets by mixing ~0.5 mg of sample, purified under the binocular microscope and verified by XRD, in 150 mg of KBr. Spectra were collected in the $4000-400$ cm$^{-1}$ MIR (mid-infrared) range by co-adding 128 scans with a 4 cm$^{-1}$ nominal resolution on a Nicolet Magna 760 spectrophotometer equipped with a KBr beam splitter, a globar source and a room-$T$ DGTS detector. Single-crystal FTIR spectra in the NIR (near infrared) range were obtained from a small cleavage fragment, ~20 μm thick, using a Bruker Hyperion 3000 microscope, equipped with an MCT (mercury-cadmium-telluride) detector in the $7500-4000$ cm$^{-1}$ range by co-adding 128 scans with a 4 cm$^{-1}$ nominal resolution.

Single-crystal Raman spectra were obtained using a confocal Horiba Jobin Yvon Labram HR Evolution spectrometer equipped with an Olympus BX41 optical microscope and a multi-channel air-cooled charge-coupled device (CCD) detector. Unpolarized Raman spectra were excited with the He-Ne 632.8 nm line. The laser power was decreased to <1 mW to avoid potential local heating effects due to heavy light absorption. The sample was inspected optically for any laser damage, and none was observed. Spectra were recorded over the wavenumber range 10 to 4000 cm$^{-1}$ using an Ultra Low Frequency (ULF) filter. The wavenumber accuracy was ±0.5 cm$^{-1}$, and the spectral resolution was <1 cm$^{-1}$. Baseline subtraction and peak fitting were performed using *GRAMS/32* software (Galactic Industries Ltd, Salem, New Hampshire, USA).

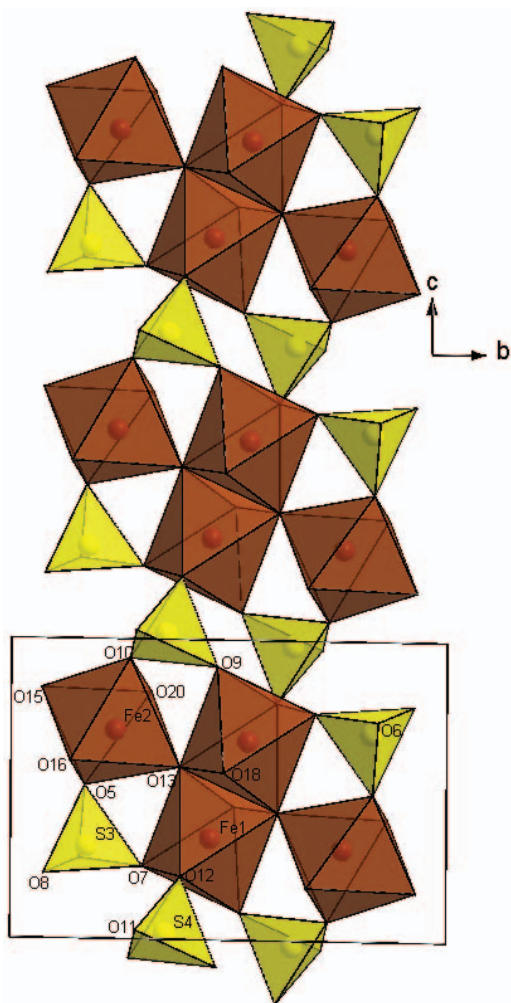## The crystal structure of hohmannite

Hohmannite is related to amarantite, $Fe_2^{3+}[O(SO_4)_2]\cdot7H_2O$ and metahohmannite, $Fe_2^{3+}[O(SO_4)_2]\cdot4H_2O$ (Bandy, 1938; Strunz and

TABLE 2. Crystallographic coordinates and displacement parameters (Å$^2$) for non-hydrogen atoms in hohmannite.

| Atom | $x$ | $y$ | $z$ | $U_{iso}$ | $U^{11}$ | $U^{22}$ | $U^{33}$ | $U^{23}$ | $U^{13}$ | $U^{12}$ |
|---|---|---|---|---|---|---|---|---|---|---|
| Fe1 | 0.40222(2) | 0.45707(2) | 0.33834(3) | 0.0132(1) | 0.01412(8) | 0.01191(8) | 0.01111(8) | −0.00013(6) | −0.00076(6) | 0.00003(6) |
| Fe2 | 0.66913(3) | 0.76067(2) | 0.30451(3) | 0.0146(1) | 0.01654(9) | 0.01175(8) | 0.01194(8) | 0.00038(6) | 0.00023(6) | −0.00124(7) |
| S3 | 0.14032(4) | 0.17441(4) | 0.30892(5) | 0.0157(1) | 0.01514(14) | 0.01352(14) | 0.01436(14) | −0.00162(11) | −0.00134(11) | −0.00182(11) |
| S4 | 0.59142(4) | 0.35448(3) | 0.01969(5) | 0.0134(1) | 0.01497(14) | 0.01293(13) | 0.01162(13) | 0.00035(10) | −0.00028(10) | 0.00330(11) |
| O5 | 0.16357(16) | 0.16955(13) | 0.51212(17) | 0.0261(6) | 0.0250(6) | 0.0285(6) | 0.0144(5) | 0.0003(4) | −0.0030(4) | −0.0075(5) |
| O6 | 0.97969(16) | 0.15706(14) | 0.2686(2) | 0.0284(6) | 0.0172(5) | 0.0269(6) | 0.0357(7) | −0.0006(5) | −0.0054(5) | −0.0014(5) |
| O7 | 0.23354(15) | 0.30203(12) | 0.24307(18) | 0.0221(5) | 0.0236(6) | 0.0155(5) | 0.0195(5) | 0.0007(4) | −0.0018(4) | −0.0056(4) |
| O8 | 0.19269(18) | 0.07563(13) | 0.21166(2) | 0.0279(7) | 0.0381(8) | 0.0197(6) | 0.0254(6) | −0.0027(5) | 0.0054(5) | 0.0077(5) |
| O9 | 0.35349(16) | 0.52742(13) | 0.08989(18) | 0.0243(5) | 0.0256(6) | 0.0202(5) | 0.0201(5) | 0.0081(4) | −0.0051(4) | −0.0039(4) |
| O10 | 0.55299(15) | 0.72765(13) | 0.06396(17) | 0.0235(5) | 0.0250(6) | 0.0212(5) | 0.0157(5) | 0.0016(4) | −0.0053(4) | −0.0060(4) |
| O11 | 0.70509(18) | 0.28674(16) | 0.0294(2) | 0.0306(8) | 0.0348(8) | 0.0381(8) | 0.0283(7) | −0.0017(6) | 0.0004(6) | 0.0255(7) |
| O12 | 0.56049(14) | 0.38986(13) | 0.21013(16) | 0.0197(5) | 0.0214(5) | 0.0254(6) | 0.0131(4) | −0.0042(4) | −0.0012(4) | 0.0081(4) |
| O13 | 0.55748(13) | 0.61234(10) | 0.42567(15) | 0.0144(4) | 0.0162(4) | 0.0117(4) | 0.01174(4) | 0.0010(3) | −0.0008(3) | −0.0015(3) |
| O14 | 0.7418(3) | 0.2431(2) | 0.4471(3) | 0.0499(12) | 0.0485(12) | 0.0387(10) | 0.0640(14) | 0.0003(10) | 0.0193(10) | 0.0145(9) |
| O15 | 0.77807(18) | 0.92986(13) | 0.16374(19) | 0.0294(6) | 0.0370(8) | 0.0202(6) | 0.0170(5) | 0.0022(4) | −0.0009(5) | −0.0129(5) |
| O16 | 0.53901(19) | 0.86434(14) | 0.4068(2) | 0.0287(7) | 0.0361(8) | 0.0235(6) | 0.0295(7) | 0.0052(5) | 0.0110(6) | 0.0129(6) |
| O17 | 0.4882(3) | 0.0398(2) | 0.1897(3) | 0.0439(11) | 0.0538(12) | 0.0425(10) | 0.0448(10) | 0.0145(8) | 0.0121(9) | 0.0278(9) |
| O18 | 0.22425(17) | 0.51219(15) | 0.4441(2) | 0.0281(7) | 0.0217(6) | 0.0304(7) | 0.0330(7) | −0.0086(6) | −0.0009(5) | 0.0091(5) |
| O19 | 0.1124(2) | 0.80474(17) | 0.2176(3) | 0.0386(9) | 0.0276(7) | 0.0276(7) | 0.0592(12) | −0.0045(8) | 0.0077(7) | 0.0061(6) |
| O20 | 0.81760(17) | 0.67875(15) | 0.1759(2) | 0.0280(7) | 0.0208(6) | 0.0324(7) | 0.0283(7) | −0.0102(6) | 0.0001(5) | 0.0045(5) |
| O21 | 0.9830(3) | 0.4760(3) | 0.2061(4) | 0.0669(16) | 0.0421(12) | 0.0652(16) | 0.0878(19) | 0.0013(14) | −0.0164(12) | 0.0081(11) |

Table 3. Experimental and calculated coordinates for hydrogen atoms in hohmannite.

| Atom | $x$ | $y$ | $z$ |
|------|------|------|------|
| H22 | 0.795(4) | 0.229(4) | 0.538(4) |
|      | 0.7707 | 0.2289 | 0.6771 |
| H23 | 0.788(4) | 0.222(4) | 0.357(4) |
|      | 0.8133 | 0.2222 | 0.535 |
| H24 | 0.791(4) | 0.923(3) | 0.052(3) |
|      | 0.7828 | 0.9296 | 0.0296 |
| H25 | 0.842(3) | 0.986(3) | 0.202(4) |
|      | 0.8469 | 0.0083 | 0.217 |
| H26 | 0.519(3) | 0.917(3) | 0.337(4) |
|      | 0.5288 | 0.9377 | 0.3341 |
| H27 | 0.460(3) | 0.838(3) | 0.459(4) |
|      | 0.4480 | 0.8282 | 0.4811 |
| H28 | 0.418(3) | 0.067(4) | 0.208(5) |
|      | 0.3979 | 0.0670 | 0.2065 |
| H29 | 0.516(4) | 0.054(4) | 0.099(4) |
|      | 0.552 | 0.0862 | 0.0939 |
| H30 | 0.152(3) | 0.503(3) | 0.372(4) |
|      | 0.1335 | 0.4942 | 0.3612 |
| H31 | 0.239(3) | 0.579(2) | 0.491(4) |
|      | 0.2442 | 0.5942 | 0.5064 |
| H32 | 0.166(4) | 0.782(3) | 0.144(4) |
|      | 0.1796 | 0.779 | 0.1355 |
| H33 | 0.124(4) | 0.876(2) | 0.213(5) |
|      | 0.1322 | 0.8966 | 0.2214 |
| H34 | 0.904(3) | 0.708(3) | 0.188(4) |
|      | 0.9204 | 0.7224 | 0.1931 |
| H35 | 0.797(3) | 0.657(3) | 0.076(3) |
|      | 0.7906 | 0.6449 | 0.0519 |
| H36 | 0.960(5) | 0.429(4) | 0.108(4) |
|      | 0.9418 | 0.404 | 0.1204 |
| H37 | 0.904(5) | 0.494(4) | 0.242(6) |
|      | 0.9081 | 0.5122 | 0.2414 |



Fig. 1. Crystal structure of hohmannite viewed along the $a$ axis.

Nickel, 2001; Scordari *et al.*, 2004), and is based structurally on polymerization of centrosymmetrical groups with composition $[Fe_4(H_2O)_8O_2(SO_4)_4]$. These minerals differ chemically in the amount of interstitial $H_2O$ groups, which also result in different packing of the sulfate chains. The structure of hohmannite (Fig. 1), in particular, is characterized by two crystallographically non-equivalent Fe sites, Fe1 and Fe2, surrounded by oxygen and water molecules to form $[Fe1O_5(H_2O)]$ and $[Fe2O_3(3H_2O)]$ octahedra, respectively. Two centrosymmetrically related $[Fe1O_5(H_2O)]$ octahedra share one edge $(O13-\overline{O13})$, whereas two additional centrosymmetrically related $[Fe2O_3(3H_2O)]$ octahedra link to either end of the shared edges. Two symmetrically unrelated $SO_4^{2-}$ groups join the Fe octahedral by

corner sharing to form $[Fe_4(H_2O)_8O_2(SO_4)_4]$ clusters that polymerize through the O12 oxygen to form complex chains of Fe−O−S linkages running along the $c$ axis. Adjacent chains are linked together by hydrogen bonds involving both the four water molecules belonging to the cluster and the four additional interstitial ($H_2O$) groups.

The positions of hydrogen atoms found here by difference Fourier (Table 3) confirm that the oxygen atoms O15, O16, O18 and O20 are water molecules linked to $Fe^{3+}$ ions, whereas the oxygen atoms O14, O17, O19 and O21 are interstitial water molecules. Inspection of the data shows that all H⋯O distances are reasonable

15

Table 4. Selected interatomic distances (Å) for the crystal structure of hohmannite.

| | | | |
|---|---|---|---|
| Fe1−O7 | 2.029(1) | Fe2−O5* | 1.978(1) |
| Fe1−O9 | 2.054(1) | Fe2−O10 | 1.998(1) |
| Fe1−O12 | 2.035(1) | Fe2−O13 | 1.869(1) |
| Fe1−O13 | 1.954(1) | Fe2−O15 | 2.099(1) |
| Fe1−$\overline{O13}$* | 1.947(1) | Fe2−O16 | 2.013(2) |
| Fe1−O18 | 2.049(2) | Fe2−O20 | 2.060(2) |
| <Fe1−O> | 2.011 | <Fe2−O> | 2.003 |
| | | | |
| S3−O5 | 1.483(1) | S4−O9* | 1.479(1) |
| S3−O6 | 1.449(1) | S4−O10* | 1.476(1) |
| S3−O7 | 1.487(1) | S4−O11 | 1.447(1) |
| S3−O8 | 1.464(2) | S4−O12 | 1.477(1) |
| <S3−O> | 1.471 | <S4−O> | 1.470 |

Notes: * $-x,-y,-z$

and that all H atoms are involved in hydrogen bonds (Table 5).

Bond-valence sums were calculated using the electrostatic strength function of Brown and Altermatt (1985) and the bond-valence parameters of Breese and O'Keeffe (1991) for all the non-H atoms refined in the present study, and bearing in mind the H-bond contributions on the basis of the H⋯O computed distances (Ferraris and Ivaldi, 1988). Table 6 shows that, excluding the contribution of the hydrogen atoms to the bond-valence calculations, the bond-valence sum (in vu, valence units) for O6, O8 and O11 (1.60, 1.54 and 1.61, respectively) is significantly less than the ideal value of 2 vu. When the hydrogen atoms are included in these calculations, the bond-valence sum becomes much more satisfactory. These calculations confirm that: (1) O6, O8

Table 5. Hydrogen-bond geometry.

| D−H⋯A | D−H (Å) | H⋯A (Å) | D⋯A (Å) |
|---|---|---|---|
| O14−H22⋯O19* | 0.86(2) | 2.03(3) | 2.878(3) |
| O14−H23⋯O6 | 0.85(2) | 2.17(3) | 2.921(3) |
| O15−H24⋯O8* | 0.82(2) | 1.95(3) | 2.762(2) |
| O15−H25⋯O6[†] | 0.76(2) | 1.97(3) | 2.710(2) |
| O16−H26⋯O17[†] | 0.82(2) | 1.81(3) | 2.632(2) |
| O16−H27⋯O14* | 0.79(2) | 1.93(3) | 2.714(3) |
| O17−H28⋯O8 | 0.79(2) | 2.09(3) | 2.852(3) |
| O17−H29⋯O17* | 0.71(2) | 2.30(3) | 2.896(4) |
| O18−H30⋯O21** | 0.82(2) | 1.89(3) | 2.712(3) |
| O18−H31⋯O14* | 0.78(2) | 1.94(3) | 2.708(3) |
| O19−H32⋯O11* | 0.81(2) | 2.02(3) | 2.827(2) |
| O19−H33⋯O8[†] | 0.76(2) | 2.08(3) | 2.831(2) |
| O20−H34⋯O19[‡] | 0.76(2) | 1.89(3) | 2.647(3) |
| O20−H35⋯O7* | 0.76(2) | 2.38(3) | 3.074(3) |
| O20−H35⋯O9* | 0.76(2) | 2.38(3) | 2.993(3) |
| O21−H36⋯O21* | 0.86(2) | 2.50(4) | 3.029(5) |
| O21−H37⋯O20 | 0.85(2) | 2.43(4) | 3.042(4) |

Notes:* $= -x,-y,-z$
** $= -1+x,y,z.$
[‡] $= 1+x,y,z$
[†] $= x,1+y,z$

TABLE 6. Bond-valence analysis for the crystal structure of hohmannite.

| | O5 | O6 | O7 | O8 | O9 | O10 | O11 | O12 | O13 | O14 | O15 | O16 | O17 | O18 | O19 | O20 | O21 | Σ |
|---|---|---|---|---|---|---|---|---|---|---|---|---|---|---|---|---|---|---|
| Fe1 | | | 0.482 | | 0.451 | | | 0.474 | 0.602 | | | | | 0.457 | | | | 3.058 |
| Fe2 | 0.553 | | | | | | | | 0.592 | | 0.399 | 0.503 | | | | 0.443 | | 3.165 |
| S3 | 1.464 | 1.604 | 1.448 | 1.541 | | | | | | | | | | | | | | 6.057 |
| S4 | | | | | 1.479 | 1.492 | 1.613 | 1.488 | 0.743 | | | | | | | | | 6.072 |
| Σv | 2.017 | 1.604 | 1.930 | 1.541 | 1.930 | 2.016 | 1.613 | 1.962 | 1.937 | | 0.399 | 0.503 | | 0.457 | | 0.443 | | |
| H22 | | | | | | | | | | 0.846 | | | | | 0.154 | | | 1.000 |
| H23 | | 0.129 | | | | | | | | 0.871 | | | | | | | | 1.000 |
| H24 | | | | 0.171 | | | | | | | 0.829 | | | | | | | 1.000 |
| H25 | | 0.167 | | | | | | | | | 0.833 | | | | | | | 1.000 |
| H26 | | | | | | | | | | | | 0.793 | 0.207 | | | | | 1.000 |
| H27 | | | | | | | | | | 0.176 | | 0.824 | | | | | | 1.000 |
| H28 | | | | 0.143 | | | | | | | | | 0.857 | | | | | 1.000 |
| H29 | | | | | | | | | | | | | 0.109 / 0.891 | | | | | 1.000 |
| H30 | | | | | | | | | | | | | | 0.814 | | | 0.186 | 1.000 |
| H31 | | | | | | | | | | 0.174 | | | | 0.826 | | | | 1.000 |
| H32 | | | | 0.148 | | | | | | | | | | | 0.852 | | | 1.000 |
| H33 | | | | | | | 0.156 | | | | | | | | 0.844 | | | 1.000 |
| H34 | | | | | | | | | | | | | | | 0.186 | 0.814 | | 1.000 |
| H35 | | | 0.100 | | 0.100 | | | | | | | | | | | 0.800 | | 1.000 |
| H36 | | | | | | | | | | | | | | | | | 0.086 / 0.914 | 1.000 |
| H37 | | | | | | | | | | | | | | | | 0.093 | 0.907 | 1.000 |
| ΣH | 2.017 | 1.900 | 2.030 | 2.003 | 2.030 | 2.016 | 1.769 | 1.962 | 1.937 | 2.067 | 2.061 | 2.120 | 2.064 | 2.097 | 2.036 | 2.150 | 2.093 | |

Notes: Values are expressed in valence units (vu). Bond strengths calculated from Breese and O'Keeffe (1991) and Ferrarsi and Ivaldi (1988).

17

and O11 are indeed the acceptor atoms for the hydrogen atoms; (2) the interstitial water molecules O14, O17, O19 and O21 act simultaneously as donors and acceptors; and (3) the refined model, as well as the location for the hydrogen atoms, are correct. A reliable hydrogen-bonding scheme according to the converging results obtained from the different techniques quoted above is illustrated in Fig. 2. The bond-valence results are consistent with the previous study (Scordari, 1978) except for some details. In our scheme the O20−H35 hydrogen bond is probably bifurcated because H35 is almost equidistant from both O7 and O9. Finally, unlike the model proposed by Scordari (1978), the O21 water group acts as donors towards $\overline{O20}$ and O20. These structural data have been tested by making use of the density-functional-based energy minimization calculations. The hydrogen positions found with both techniques are converging (Table 3) even if the calculated O−H bonds (0.95−0.98 Å) are longer than the corresponding ones derived from the difference Fourier map (0.71(2)−0.86(2) Å). These differences are not unexpected and can be explained readily. The theoretical values, in fact, concern distances between nuclear positions, while the experimental values from XRD experiments measure distances between the centroids of the electron density; in the latter case it is reasonable to expect the electron density of hydrogen to be shifted markedly towards the bonding atom.

## Infrared and Raman spectroscopy

The powder FTIR spectrum of hohmannite in the MIR 4000−400 cm$^{-1}$ range is displayed in Fig. 3; measured band positions (wavenumbers, cm$^{-1}$) are listed in Table 7, where the band assignments are based on literature data for similar materials (e.g. Omori and Kerr, 1963; Adler and Kerr, 1965; Bishop *et al.*, 2004; Cloutis *et al.*, 2006; Ross, 1974; Lane, 2007; Della Ventura *et al.*, 2013).

In the higher wavenumber, water-stretching region (>2500 cm$^{-1}$) a very broad absorption extending from 3700 to 2800 cm$^{-1}$ (Fig. 3) is observed; it peaks around 3438 cm$^{-1}$ with a shoulder at 3234 cm$^{-1}$. This broad band is evidently due to the contribution of several overlapping components, including the overtone of the H$_2$O bending mode ($2 \cdot v_2$) expected around 3250 cm$^{-1}$. The unpolarized spectrum collected on a single crystal in the NIR range (Fig. 4), shows a relatively broad and intense absorption due to the ($v_3$ + $v_2$) H$_2$O combination at 5115−5230 cm$^{-1}$. No bands are observed in the 4000−4500 cm$^{-1}$ range, ruling out any presence
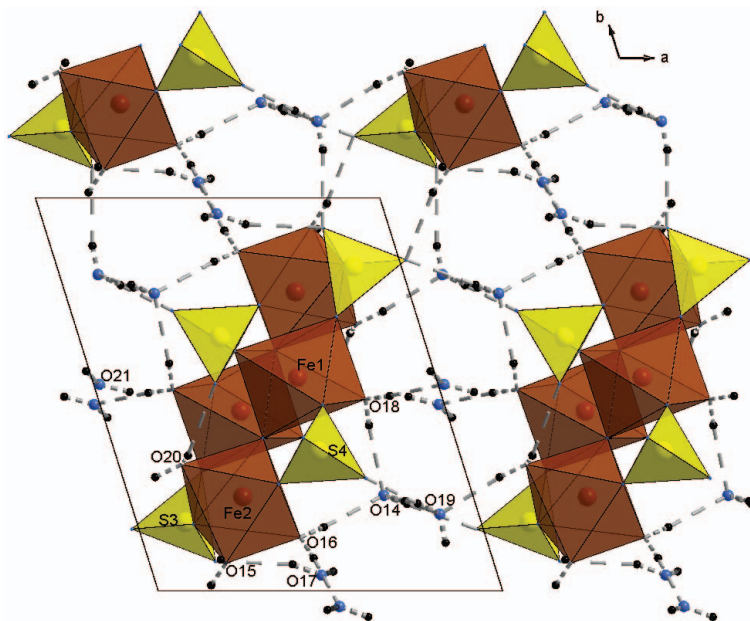


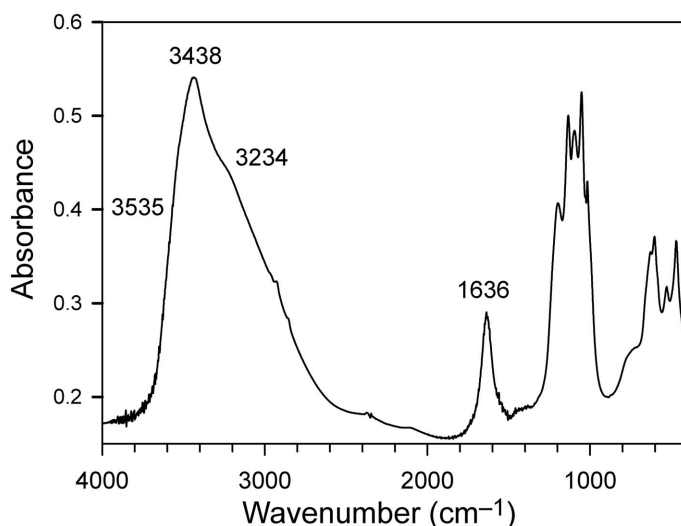FIG. 2. The hydrogen-bonding system of hohmannite.

18

FIG. 3. Room temperature FTIR powder spectrum of hohmannite in the MIR 4000−400 cm$^{-1}$ region.

of hydroxyl groups in the structure. The first $H_2O$ overtone ($2 \cdot v_3$) band is observed as a broad and unresolved absorption centred around 6920 cm$^{-1}$.

In the hohmannite structure there are eight independent $H_2O$ molecules (Fig. 2); these are involved in hydrogen bonds of different strengths with the surrounding oxygens (Table 5), thus reducing their local $C_{2v}$ ideal symmetry (e.g. Nakamoto, 1997). As a consequence, each O−H bond in the $H_2O$ molecule vibrates independently with a frequency related to the local strength of hydrogen bonding. If eight $H_2O$ molecules are considered, 16 asymmetric stretching bands are expected and these overlap to give the broad pattern of Fig. 3. According to the data of Table 5, in the hohmannite structure the different O−H$\cdots$O hydrogen bond lengths vary in the range 2.632−3.074 Å. If the empirical $O_{donor} \cdots O_{acceptor}$ distance–frequency correlation of Libowitzky (1999) is considered, bands covering a broad range of frequency are expected, between 3500 and 3000 cm$^{-1}$, and this is what is observed (Fig. 3). The $H_2O$ bending mode occurs as a relatively broad absorption centred at 1636 cm$^{-1}$ (Fig. 3). The Raman spectrum shows a very weak and broad absorption in the water-

TABLE 7. Positions (wavenumber, cm$^{-1}$) and proposed assignment for peaks observed in the FTIR and Raman spectra of hohmannite.

| Infrared | Raman | Assignment |
|---|---|---|
| 3438, 3234 | 3495, 3438, 3292, 3204 | $v_3(H_2O)$, $2 \cdot v_2(H_2O)$ |
| 1636 | | $v_2(H_2O)$ |
| 1198, 1134, 1096, 1052 | 1204, 1166, 1125, 1098, 1075, 1058 | $v_3(SO_4)$ antisymmetric stretching |
| 1028, 1016 | 1031, 1018 | $v_1(SO_4)$ symmetric stretching |
| 659, 629, 604, 529 | 659, 628, 605, 580 | $v_4(SO_4)$ antisymmetric bending |
| 470 | 496, 470<br>400, 334, 258, 245, 227<br>198, 163, 144, 129, 73, 49 | $v_2(SO_4)$ symmetric bending<br>Fe−O,OH modes<br>Lattice modes |

19
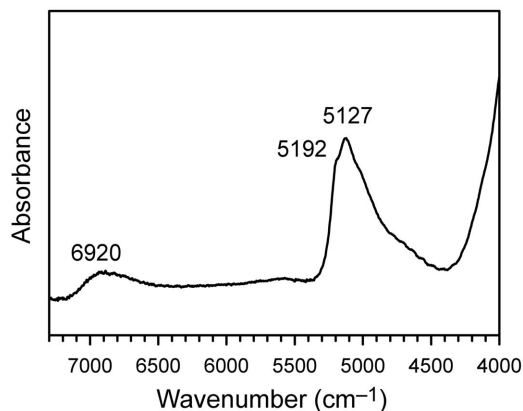
FIG. 4. Single-crystal unpolarized spectrum of hohmannite in the NIR region.

stretching $\nu_3(F_2)$ at 1105 cm$^{-1}$ and the anti-symmetric bending $\nu_4(F_2)$ at 611 cm$^{-1}$ (e.g. Adler and Kerr, 1965; Ross, 1974). In accordance with selection rules, all modes are either Raman alone or Raman and IR active; there are no IR active only or inactive vibrations. In particular, the $A_1$ non-degenerate symmetric stretching and the doubly degenerate $E$ symmetric bending modes are Raman active only, whereas the triply degenerate asymmetric $F_2$ stretching and bending modes are both Raman- and infrared-active (Table 8). In a solid sulfate structure, however, the arrangement of the surrounding cations causes distortion of the $SO_4$ polyhedra away from the $T_d$ site configuration (Adler and Kerr, 1965; Ross, 1974; Della Ventura *et al.*, 2013). As a consequence of this symmetry reduction, we typically observe in the IR pattern a shift of the absorption bands to different energies, the removal of degeneracy (band splitting) and modification in the spectral activity (appearance of ideally non-active IR/Raman modes).

According to Table 8, where a correlation table for the fundamental vibrations of the $SO_4^{2-}$ group in hohmannite, point group $C_1$, is presented, 6 IR + 6 Raman bands are expected as both $\nu_3$ and $\nu_4$ modes, whereas 2 IR + 2 Raman and 1 IR + 1 Raman bands are expected as $\nu_2$ and $\nu_1$ modes, respectively. Examination of Fig. 6 and

stretching region (Fig. 5) with two components peaked at 3438 and 3204 cm$^{-1}$, and two evident shoulders at 3495 and 3292 cm$^{-1}$, respectively.

The powder FTIR spectrum in the low-frequency 1400−400 cm$^{-1}$ region is given in Fig. 6 in comparison with the Raman spectrum, collected down to 10 cm$^{-1}$. It is well known that a free $SO_4^{2-}$ ion with ideal $T_d$ symmetry has four modes of vibration (Table 8): the symmetric stretching $\nu_1(A_1)$ at 983 cm$^{-1}$, the symmetric bending $\nu_2(E)$ at 450 cm$^{-1}$, the antisymmetric
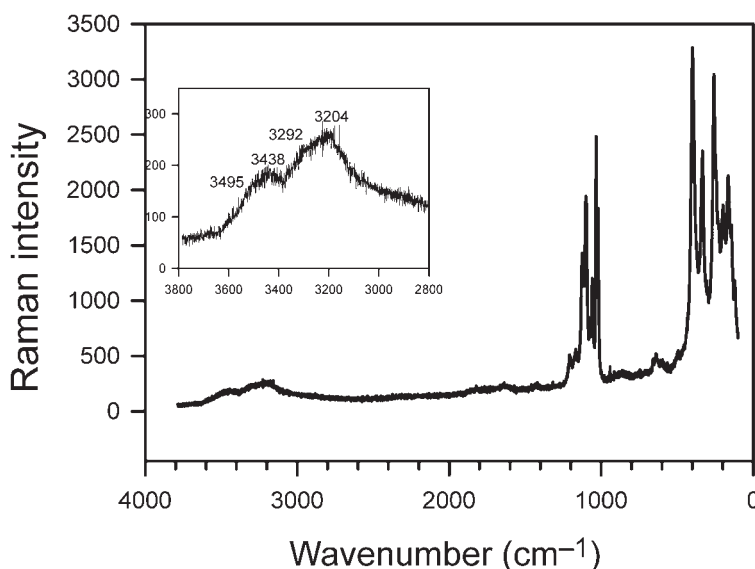


FIG. 5. Unpolarized single-crystal Raman spectrum of hohmannite in the full 4000−20 cm$^{-1}$ frequency range. The H$_2$O stretching region is magnified in the inset.
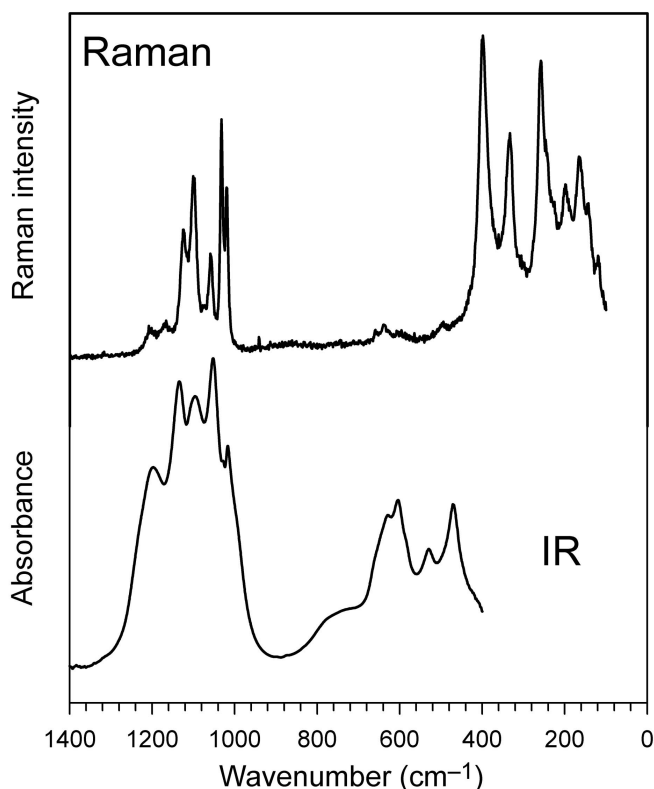
20

FIG. 6. Comparison between the powder FTIR spectrum and the single-crystal Raman spectrum of hohmannite in the low-frequency region.

Table 7 shows that most of the expected bands are indeed present in the spectra although, due to severe overlapping, some of them appear as shoulders only. In the FTIR pattern, four intense bands are observed in the antisymmetric stretching range at 1198, 1134, 1096 and 1052, while two components at 1028 and 1016 occur as symmetric stretching modes. In the Raman spectrum, three weak bands at 1204, 1166 and 1075, and three intense bands at 1125, 1098 and 1058 cm$^{-1}$ are present, while the $\nu_1$ modes occur as an intense doublet at 1031 and 1018 cm$^{-1}$. It is to be noted that, although this mode for the ($SO_4^{2-}$) group is non degenerate (Table 8, see also Adler and Kerr, 1965), the presence of two components in both IR and Raman spectra is in agreement with two independent sulfate sites in the hohmannite structure (Scordari, 1978; this work). The antisymmetric bending modes ($\nu_4$) are strong in the IR spectrum whereas they are very weak in the Raman

TABLE 8. SO$_4$ internal mode analysis in hohmannite by the correlation method.

| SO$_4$ internal mode | Free ion point group $T_d$ | Site symmetry $C_1$ | Space group $P\bar{1}$ ($C_i$) | |
|---|---|---|---|---|
| $\nu_1$ | $A_1$ | $A$ | $A_g+A_u$ | $A_g$ (Raman active) |
| $\nu_2$ | $E$ | $2A$ | $2A_g+2A_u$ | $A_u$ (IR active) |
| $\nu_3$ | $F_2$ | $3A$ | $3A_g+3A_u$ | |
| $\nu_4$ | $F_2$ | $3A$ | $3A_g+3A_u$ | |

21

pattern. The measured Raman range extends at very low wavenumbers ($\leqslant 10$ cm$^{-1}$) allowing the identification of $\nu_2$ (SO$_4^{2-}$), Fe$-$O, H$_2$O and lattice modes, following the assignments from previous studies in the literature on sulfates. The $\nu_2$ (SO$_4^{2-}$) modes are observed at wavenumbers >400 cm$^{-1}$ (e.g. Ross, 1974; Knittle *et al.*, 2001; Murphy *et al.*, 2009; Frost *et al.*, 2013) in the Raman spectrum as very intense absorptions (Fig. 6). Vibrational analysis by the application of the correlation method yields six modes that are Raman active ($6\,A_\mathrm{g} + 6\,A_\mathrm{u}$). The unequivocal assignment of these modes is difficult due to the concomitant occurrence in this spectral range of $\nu_2$(SO$_4^{2-}$) and Fe$-$O,OH modes (Frost *et al.*, 2013; Murphy *et al.*, 2009). Nevertheless, these low wavenumber modes are assigned to the Raman peaks located between 400 and 227 cm$^{-1}$. Finally, Raman peaks that are found below 200 cm$^{-1}$ can generally be classified as lattice modes (e.g. Frost *et al.*, 2004, 2013).

## Conclusion

A new and more accurate structure refinement of the rare Fe sulfate, hohmannite, is reported here, where the hydrogen-bonding scheme has been characterized due to improved XRD data, and confirmed by periodic *ab initio* calculations. The first vibrational spectroscopic (FTIR + Raman) data for this phase are also reported. The spectra in the principal H$_2$O stretching region show a multicomponent broad band in the 3700$-$2800 cm$^{-1}$ frequency range compatible with the empirical O$_\mathrm{donor}$$\cdots$O$_\mathrm{acceptor}$ distance-frequency correlation of Libowitzky (1999) based on the structure refinement. Comparison with the spectroscopic data found in the literature (e.g. Omori and Kerr, 1963; Adler and Kerr, 1965; Ross, 1974; Bishop *et al.*, 2004; Cloutis *et al.*, 2006; Lane, 2007; Della Ventura *et al.*, 2013) shows that the vibrational spectra of hohmannite, in particular in the low-frequency (1400$-$440 cm$^{-1}$) region, allow us to distinguish this species from other Fe sulfates. For example, as mentioned above hohmannite may occur associated with amarantite and butlerite. Both FTIR and Raman spectra obtained for hohmannite are significantly different from published spectra of amarantite (Frost *et al.*, 2013) and butlerite/parabutlerite (Cejka *et al.*, 2011). The distinction between hohmannite and metahohmannite based on spectroscopic data is, however, much more subtle. The behaviour of hohmannite at high temperature has been examined recently and its decomposition products studied by using a combination of thermogravimetric, XRD and FTIR data (Ventruti *et al.*, 2015). The powder FTIR spectrum observed is not significantly modified in the lower-frequency (<1300 cm$^{-1}$) region across the hohmannite–metahohmannite transition which occurs at ~120ºC (Scordari *et al.*, 2004, Ventruti *et al.*, 2015). However, the FTIR spectrum in the NIR (4000$-$5000 cm$^{-1}$) region is extremely sensitive to the modification in the H$_2$O content of the sulfate phase, and can thus be used to distinguish between these two sulfate compounds. Despite these difficulties we remain convinced that it is worth attempting to improve spectroscopic methods to characterize these minerals.

## Acknowledgements

## References

Adler, H.H. and Kerr, P.F. (1965) Variations in infrared spectra, molecular symmetry and site symmetry of sulfate minerals. *American Mineralogist*, **50**, 132$-$147.

Bandy, M.C. (1938) Mineralogy of three sulphate deposits of Northern Chile. *American Mineralogist*, **23**, 669$-$760.

Betteridge, P.W., Carruthers, J.R., Cooper, R.I., Prout, K. and Watkin, D.J. (2003) Crystals version 12: Software for guided crystal structure analysis. *Journal of Applied Crystallography*, **36**, 1487.

Bishop, J.L., Dyar, M.D., Lane, M.D. and Banfield, J. (2004) Spectral identification of hydrated sulfates on Mars and comparison with acidic environments on Earth. *International Journal of Astrobiology*, **3**, 275$-$285.

Blessing, R.H. (1995) An empirical correction for absorption anisotropy. *Acta Crystallographica*, **A51**, 33$-$38.

Breese, N.E. and O'Keeffe, M. (1991) Bond-valence parameters for solids. *Acta Crystallographica*, **B47**, 192$-$197.

Brown, I.D. and Altermatt, D. (1985) Bond valence parameters obtained from a systematic analysis of the inorganic crystal structure database. *Acta Crystallographica*, **B41**, 244$-$247.

Bruker (2008) APEX2, SAINT and TWINABS. Bruker AXS Inc., Madison,Wisconsin, USA.

Burns, R.G. (1987) Ferric sulfates on Mars. Pp. E570−E574 in: *Journal of Geophysical Research, Proceedings of the seventeenth Lunar and Planetary Science Conference*, *Part 2*. **Vol. 92, No. B4**, Houston, Texas, USA, 30 March 1987. American Geophysical Union, Washington, DC.

Cejka, J., Sejkora, J., Plasil, J., Bahfenne, S., Palmer, Sara, J., Rintoul, L. and Frost, R.L. (2011) A vibrational spectroscopic study of hydrated $Fe^{3+}$ hydroxyl-sulphates; polymorphic minerals butlerite and parabutlerite. *Spectrochimica Acta A*, **79**, 1356−1363.

Cloutis, E.A., Hawthorne, F.C., Mertzman, S.A., Krenn, K., Craig, M.A., Marcino, D., Methot, M., Strong, J., Mustard, J.F., Blaney, D.L., Bell III, J.F. and Vilas, F. (2006) Detection and discrimination of sulphate minerals using reflectance spectroscopy. *Icarus*, **184**, 121−157.

Della Ventura, G., Ventruti, G., Bellatreccia, F., Scordari, F. and Cestelli Guidi, M. (2013) FTIR transmission spectroscopy of sideronatrite, a sodium-iron hydrous sulfate. *Mineralogical Magazine*, **77**, 499−507.

Ferraris, G. and Ivaldi, G. (1988) Bond valence *vs* bond length in O···O hydrogen bonds. *Acta Crystallographica*, **B44**, 341−344.

Frost, R.L., Williams, P.A., Martens, W., Leverett, P. and Kloprogge, J.T. (2004) Raman spectroscopy of basic copper(II) and some complex copper(II) sulfate minerals: implications for hydrogen bonding. *American Mineralogist*, **89**, 1130−1137.

Frost, R.L., López, A., Scholz, R., Xi, Y., da Silveira, A.J. and Fernandes Lima, R.M. (2013) Characterization of the sulphate mineral amarantite − $Fe_2^{3+}(SO_4)_2O\cdot7H_2O$ using infrared, Raman spectroscopy and thermogravimetry. *Spectrochimica Acta A*, **114**, 85−91.

Jerz, J.K. and Rimstidt, J.D. (2003) Efflorescent iron sulfate minerals: Paragenesis, relative stability, and environmental impact. *American Mineralogist*, **88**, 1919−1932.

Johnson, J.R., Bell, J.F., Cloutis, E., Staid, M., Farrand, W.H., McCoy, T., Rice, M., Wang, A. and Yen, A. (2007) Mineralogic constraints on sulfur-rich soils from Pancam spectra at Gusev crater, Mars. *Geophysical Research Letters*, **34**, L13202.

Klingelhöfer, G., Morris, R.V., Bernhardt, B. and Schröde, C. (2004) Jarosite and hematite at Meridiani Planum from Opportunity's Mössbauer spectrometer. *Science*, **306**, 1740−1745.

Knittle, E., Phillips, W. and Williams, G. (2001) An infrared and Raman spectroscopic study of gypsum at high pressure. *Physics and Chemistry of Minerals*, **28**, 630−640.

Lane, M.D. (2007) Mid-infrared emission spectroscopy of sulfate and sulfate-bearing minerals. *American Mineralogist*, **92**, 1−18.

Lane, M.D., Bishop, J.L., Dyar, M.D., King, P.L., Parente, M. and Hyde, B.C. (2008) Mineralogy of the Paso Robles soils on Mars. *American Mineralogist*, **93**, 728−739.

Libowitzky, E. (1999) Correlation of O−H stretching frequencies and O−H···O hydrogen bond lengths in minerals. *Monatshefte für Chemie*, **130**, 1047−1059.

McCollom, T.M., Ehlmann, B.L., Wang, A., Hynek, B.M., Moskowitz, B. and Berquó, T.S. (2014) Detection of iron substitution in natroalunite-natrojarosite solid solutions and potential implications for Mars. *American Mineralogist*, **99**, 948−964.

Mills, S.J., Nestola, F., Kahlenberg, V., Christy, A.G., Hejny, C. and Redhammer, G.J. (2013) Looking for jarosite on Mars: The low-temperature crystal structure of jarosite. *American Mineralogist*, **98**, 1966−1971.

Murphy, P.J., Smith, A.M.L., Hudson-Edwards, K.A., Dubbin, W.E. and Wright, K. (2009) Raman and IR spectroscopic studies of alunite-supergroup compounds containing Al, $Cr^{3+}$, $Fe^{3+}$ and $V^{3+}$ at the B site. *The Canadian Mineralogist*, **47**, 663−681.

Nakamoto, K. (1997) *Infrared and Raman Spectra of Inorganic and Coordination Compounds*. Fifth edition. Wiley and Sons, New York.

Ngenda, R.B., Segers, L. and Kongolo, P.K. (2009) *Base metals recovery from zinc hydrometallurgical plant residues by digestion method*. Hydrometallurgy Conference 2009, The Southern African Institute of Mining and Metallurgy, Johannesburg, pp. 17−29.

Nordstrom, D.K., Alpers, C.N., Ptacek, C.J. and Blowes D.W. (2000) Negative pH and extremely acidic mine waters from Iron Mountain, California. *Environmental Science and Technology*, **34**, 254−258.

Omori, K. and Kerr, P.F. (1963) Infrared studies of saline sulphate minerals. *Geological Society of America Bulletin*, **74**, 709−734.

Palache, C., Berman, H. and Frondel, C. (1951) *Dana's System of Mineralogy*. John Wiley and Sons, Inc., New York.

Ross, S.D. (1974) Sulphates and other oxy-anions of group VI. Pp. 423−444 in: *The Infrared Spectra of Minerals* (V.C. Farmer, editor), The Mineralogical Society, London.

Ruhl, A.S. and Kranzmann, A. (2012) Corrosion behavior of various steels in a continuous flow of carbon dioxide containing impurities. *International Journal of Greenhouse Gas Control*, **9**, 85−90.

Saunders, V.R., Dovesi, R., Roetti, C., Orlando, R., Zicovich-Wilson, C.M., Harrison, N.M., Doll, K., Civalleri, B., Bush, L.J., D'Arco, Ph. and Llunell, M. (2003) *CRYSTAL 2003 user's manual*. University of Torino, Turin, Italy.

Scordari, F. (1978) The crystal structure of hohmannite, $Fe_2(H_2O)_4[(SO_4)_2O]\cdot4H_2O$ and its relationship to amarantite, $Fe_2(H_2O)_4[(SO_4)_2O]\cdot3H_2O$. *Mineralogical Magazine*, **42**, 144−146.

Scordari, F., Ventruti, G. and Gualtieri, A.F. (2004) The structure of metahohmannite, $Fe_2^{3+}[O(SO_4)_2]4H_2O$, by *in situ* synchrotron powder diffraction. *American Mineralogist*, **89**, 265−370.

Strunz, H. and Nickel, E.H. (2001) *Strunz Mineralogical Tables. Chemical Structural Mineral Classification System, 9th Edition*. Schweizerbart, Stuttgart, Germany, 870 pp.

Ventruti, G., Scordari, F., Della Ventura, G., Bellatreccia, F., Gualtieri, A.F. and Lausi, A. (2013) The thermal stability of sideronatrite and its decomposition products in the system $Na_2O-Fe_2O_3-SO_2-H_2O$. *Physics and Chemistry of Minerals*, **40**, 659−670.

Ventruti, G., Della Ventura, G., Scordari, F., Susta, U. and Gualtieri, A.F. (2015) *In situ* high-temperature XRD and FTIR investigation of hohmannite, a water-rich Fe-sulfate, and its decomposition pro-ducts. *Journal of Thermal Analysis and Calorimetry*, **119**, 1793−1802.

Vicenzi, E.P., Fries, M., Fahey, A., Rost, D., Greenwood, J.P. and Steele, A. (2007) Detailed elemental, mineralogical, and isotopic examination of jarosite in Martian meteorite MIL 03346. *38th Lunar and Planetary Science Conference, (Lunar and Planetary Science XXXVIII)*, March 12−16, 2007, League City, Texas, USA. LPI Contribution No. 1338, p.2335.

Welch, S.A., Christy, A.G., Kirste, D., Beavis, S.G. and Beavis, F. (2007) Jarosite dissolution I − trace cation flux in acid sulfate soils. *Chemical Geology*, **245**, 183−197.

Welch, S.A., Kirste, D., Christy, A.G., Beavis, F.R. and Beavis, S.G. (2008) Jarosite dissolution II − reaction kinetics, stoichiometry and acid flux. *Chemical Geology*, **254**, 73−86.

Welch, S.A., Christy, A.G., Isaacson, L. and Kirste, D. (2009) Mineralogical control of rare earth elements in acid sulfate soils. *Geochimica et Cosmochimica Acta*, **73**, 44−64.